APPLIED SCIENCES AND ENGINEERING

Soft, bioresorbable, transparent microelectrode arrays for multimodal spatiotemporal mapping and modulation of cardiac physiology

Zhiyuan Chen^{1†}, Zexu Lin^{1†}, Sofian N. Obaid¹, Eric Rytkin², Sharon A. George², Christopher Bach¹, Micah Madrid¹, Miya Liu¹, Jessica LaPiano³, Amy Fehr¹, Xinyu Shi¹, Nathaniel Quirion¹, Benjamin Russo¹, Helen Knight¹, Anthony Aduwari¹, Igor R. Efimov^{2,4}*, Luyao Lu¹*

Transparent microelectrode arrays (MEAs) that allow multimodal investigation of the spatiotemporal cardiac characteristics are important in studying and treating heart disease. Existing implantable devices, however, are designed to support chronic operational lifetimes and require surgical extraction when they malfunction or are no longer needed. Meanwhile, bioresorbable systems that can self-eliminate after performing temporary functions are increasingly attractive because they avoid the costs/risks of surgical extraction. We report the design, fabrication, characterization, and validation of a soft, fully bioresorbable, and transparent MEA platform for bidirectional cardiac interfacing over a clinically relevant period. The MEA provides multiparametric electrical/optical mapping of cardiac dynamics and on-demand site-specific pacing to investigate and treat cardiac dysfunctions in rat and human heart models. The bioresorption dynamics and biocompatibility are investigated. The device designs serve as the basis for bioresorbable cardiac technologies for potential postsurgical monitoring and treating temporary patient pathological conditions in certain clinical scenarios, such as myocardial infarction, ischemia, and transcatheter aortic valve replacement.



Authors, some rights reserved; exclusive licensee American Association for the Advancement of Science. No claim to original U.S. Government Works, Distributed under a Creative Commons Attribution NonCommercial License 4.0 (CC BY-NC).

INTRODUCTION

Heart disease costs the United States ~\$219 billion annually, with ~655,000 Americans dying from heart disease each year (about one in four deaths) (1, 2). A contributing factor underlying these unexpectedly grim numbers is the lack of tools that can spatiotemporally map and control the cardiac metabolic and electromechanical activity to unravel the complex pathophysiology of heart disease, provide intraoperative or postsurgical recovery monitoring, and develop effective and timely clinical treatments. Noble metal [e.g., platinum (Pt) and iridium]-based microelectrode arrays (MEAs) are widely used to probe the patterns of cardiac excitation waves and identify the regions that are responsible for cardiac arrhythmias, while electrical cardiac pacemakers and defibrillators are the cornerstone of therapy used in clinical medicine to correct the abnormal heart rhythm (3–5). However, they are problematic in probing important cardiac parameters such as intracellular calcium dynamics, metabolic activity, or target-specific cell types. Optical mapping using voltage/calcium-sensitive fluorescent dyes or intrinsic fluorescence complements these electrical approaches and reveals the roles of the aforementioned cellular parameters during cardiac function in health and disease (6). Recent developments in optically transparent MEAs based on graphene (7, 8), carbon nanotubes (CNTs) (9), conductive polymers (10), and gold (Au) nanostructures (11, 12) have allowed light to transmit through the microelectrodes in both directions for colocalized cross-talk-free

electrophysiology and optical mapping to take the full advantages of each technique (13). In addition, optically transparent MEAs are highly desired during clinical processes to allow direct observation of areas of interest under the microelectrode sites for concurrent optical diagnostics/therapies (e.g., endoscopy) and guiding other procedures (e.g., catheters) on the hearts (14). Meanwhile, all current transparent MEAs are designed to exhibit long-term reliable performance for chronic biointerfacing (13).

In comparison, bioresorbable electronics offer unique opportunities to investigate, monitor, and treat short-lived cardiac complications, such as postoperative arrhythmias and heart failure on the order of a few days to weeks following ischemic events or surgery (15), which account for at least one-third of postoperative deaths (16). Those devices can subsequently dissolve into benign products via natural metabolic mechanisms to avoid complications from surgical retrieval of the implants, lower infection risks, and eliminate additional financial burdens to patients. For example, removal of the temporary pacing devices following completion of therapy can cause laceration and perforation of the myocardium (17). There has been much recent work on soft bioresorbable electronic devices (18-20). Examples include cardiac pacemakers to treat cardiac arrhythmias (21), peripheral nerve stimulators for pain block (22), electrical sensors to map activity from the cerebral cortex (23) or record physiological signals (24), electrotherapy systems to provide electrostimulation and impedance sensing (25), chemical sensors to monitor critical biomarkers in various organs (26), etc. However, developments in soft transparent MEAs that exhibit bioresorbable functionality remain limited and challenging.

Here, we report materials, device designs, fabrication strategies, performance characteristics, ex vivo and in vivo demonstrations, and systematic biocompatibility assessments of a fully

¹Department of Biomedical Engineering, The George Washington University, Washington, DC 20052, USA. ²Department of Biomedical Engineering, Northwestern University, Evanston, IL 60208, USA. ³MedStar Georgetown University Hospital, Washington, DC 20037, USA. ⁴Department of Medicine (Cardiology), Northwestern University, Chicago, IL 60611, USA.

^{*}Corresponding author. Email: igor.efimov@northwestern.edu (I.R.E); luyaolu@ gwu.edu (L.L)

[†]These authors contributed equally to this work.

bioresorbable, implantable, flexible, and transparent MEA technology that can provide organ conformal cardiac interfacing over clinically relevant temporary time scales. The devices integrate entirely Food and Drug Administration-approved materials that will completely disappear through natural biological processes in the body after a desired period of use. Key components include a transparent and flexible poly(lactic-co-glycolic acid) (PLGA) substrate, an electron beam lithography (EBL)-patterned transparent molybdenum (Mo) nanogrid MEA, a photolithography-determined interconnect layer, and a soft lithography-defined transparent PLGA encapsulation layer. The nanoscale Mo structures are based on our recently reported metal grid approaches for preparing high-performance soft transparent MEAs (12, 27, 28). Studies on rat and human hearts highlight the function, form factor, durability, and capability of the devices for (i) colocalized multiparametric spatiotemporal electrical/optical mapping of critical cardiac physiological parameters, such as heart rhythm, biopotentials, oxygenation, metabolic state, calcium homeostasis, activation propagation pattern, and myocardial conduction and contraction and (ii) real-time demand-based site-specific cardiac pacing to control the propagations of cardiac waves and provide therapeutic solutions such as treating bradycardia and atrioventricular (AV) block on soft heart tissue surfaces. We would like to note that alternative pacing technologies, such as optogenetic or nongenetic optical pacing of the hearts, have also been widely used in cardiac research (29-35). Optogenetics is a promising optical pacing method that uses light-activated ion channels to control cardiac activity. However, it could be challenging to implement optogenetic pacing for clinical applications because of the requirement of gene transfection. Nongenetic optical pacing techniques use materials that can convert photons into electricity or heat to modulate the membrane potentials of cardiomyocytes. Those technologies mostly rely on external light sources for optical pacing with physically separated electrocardiogram (ECG) electrodes for monitoring the resulting cardiac activity and could be difficult to accommodate concurrent optical mapping experiments due to potential optical cross-talk. Meanwhile, the MEAs in this work enable both single-site and multisite pacing with simultaneous electrical cardiac mapping in detecting and treating cardiac complications, require no genetic labels, and avoid the potential optical cross-talk with colocalized optical mapping investigations, which are more suitable for future temporary nontoxic safe use in humans. The MEAs are stable for several days when immersed in phosphate-buffered saline (PBS), which is on par with many postoperative care cycles (36, 37), followed by complete bioresorption via hydrolysis within 6 weeks in vivo. Together, this work establishes the foundations of a soft bioresorbable transparent MEA technology to greatly expand the landscape for bioresorbable transient electronics and complement traditional approaches, with the potential to address the unmet needs in fundamental and translational cardiac research [e.g., ablation and surgical intervention procedures, postoperative recovery monitoring, post-infarction recovery, and post-transcatheter aortic valve replacement (TAVR) recovery] where transient mapping and control of cardiac physiological parameters and functions are required.

RESULTS

Design of bioresorbable and transparent Mo nanogrid MEA

Figure 1A presents a schematic illustration of a 4 × 4 bidirectional MEA platform attached to the heart surface. The MEA device is transparent (Fig. 1B, left) and flexible (Fig. 1B, right). Each microelectrode features a nanogrid network structure with a thickness of 1000 nm, a grid width of 500 nm, and a pitch of 6.75 μm (Fig. 1C). The nanoscale dimensions enable adjusting the physical properties of the nanogrid network when scaling down the microelectrode sizes. The void spaces between the nanogrids allow photons to pass through the microelectrodes for colocalized optical operations. The edge-to-edge distance between two nearby microelectrodes in the MEA is determined by the electrophysiological space constant of cardiac tissue to achieve high spatial resolution electrical mapping and control of the cardiac signal propagation from the epicardium (38). The overall active MEA area (~5 mm by 5 mm) is on par with the sizes of ventricles or atria of small animals (39, 40). The entire device is thin (thickness, ~140 μm) and extremely lightweight (~16 mg). One key feature of the MEA is that it consists entirely of bioresorbable and biocompatible materials that eventually dissolve in the body. The microelectrodes and interconnects rely on Mo metal because of its relatively slow dissolution rate under physiological conditions, which could help extend the device's operational lifetime compared to other metals such as magnesium (22, 41). The PLGA (lactide:glycolide, 65:35) layer serves as the support (thickness, 90 µm) for the MEA and encapsulation (thickness, 50 μm) to define microelectrode sizes. The fabrication process appears in fig. S1 and Materials and Methods, which shows a high yield of 97% (n > 40 MEA devices). In addition to the nanoscale patterns, the fabrication process for the bioresorbable transparent MEA is versatile and also compatible with the standard photolithography process, which can generate microscale grids with programmable parameters if needed (fig. S2).

Bench testing of the 16-channel Mo nanogrid MEA

The physical and chemical properties of the Mo nanogrids could be adjusted by controlling nanogrid thickness and spacing. Figure 1D presents the transmission spectra of Mo nanogrids (grid width, 500 nm; pitch, 6.75 µm) in the visible wavelength range at various thicknesses. As the nanogrid thickness increases from 100 to 500 nm and 1000 nm, the average transmittance value at 550 nm first decreases from 84.2 \pm 1.0 to 80.0 \pm 1.5% and then stabilizes at 79.1 \pm 1.2%, respectively. Figure 1E shows the effect of nanogrid pitch (grid width, 500 nm; thickness, 1000 nm) on optical transparency. As expected, the average 550-nm transmittance value increases from 53.5 \pm 2.0 to 79.1 \pm 1.2% and 85.4 \pm 1.1% when the pitch increases from 3.5 to 6.75 µm and 14.75 µm, respectively. Overall, the bioresorbable Mo nanogrid microelectrodes exhibit excellent optical transparency to allow light transmission in both directions.

Mo dissolves into nontoxic products in aqueous environments based on the reaction: $2\text{Mo} + 2\text{H}_2\text{O} + 3\text{O}_2 \rightarrow 2\text{MoO}_4^{2-} + 4\text{H}^+$ (25, 42). Figure 1F demonstrates the dissolution kinetics and thickness profiles of the 1000-nm-thick Mo layers in 1× PBS (pH 7.4). The measured dissolution rate is 2.4, 19, and 62 nm/hour at 37°, 60°, and 90°C, respectively. At physiological temperature (37°C), ~0.3 µg of Mo dissolves per day, which is within the safe daily intake (~45 µg) (26, 43). Figure 1G demonstrates the different dissolution stages of the MEA device immersed in 1× PBS (pH 7.4 and

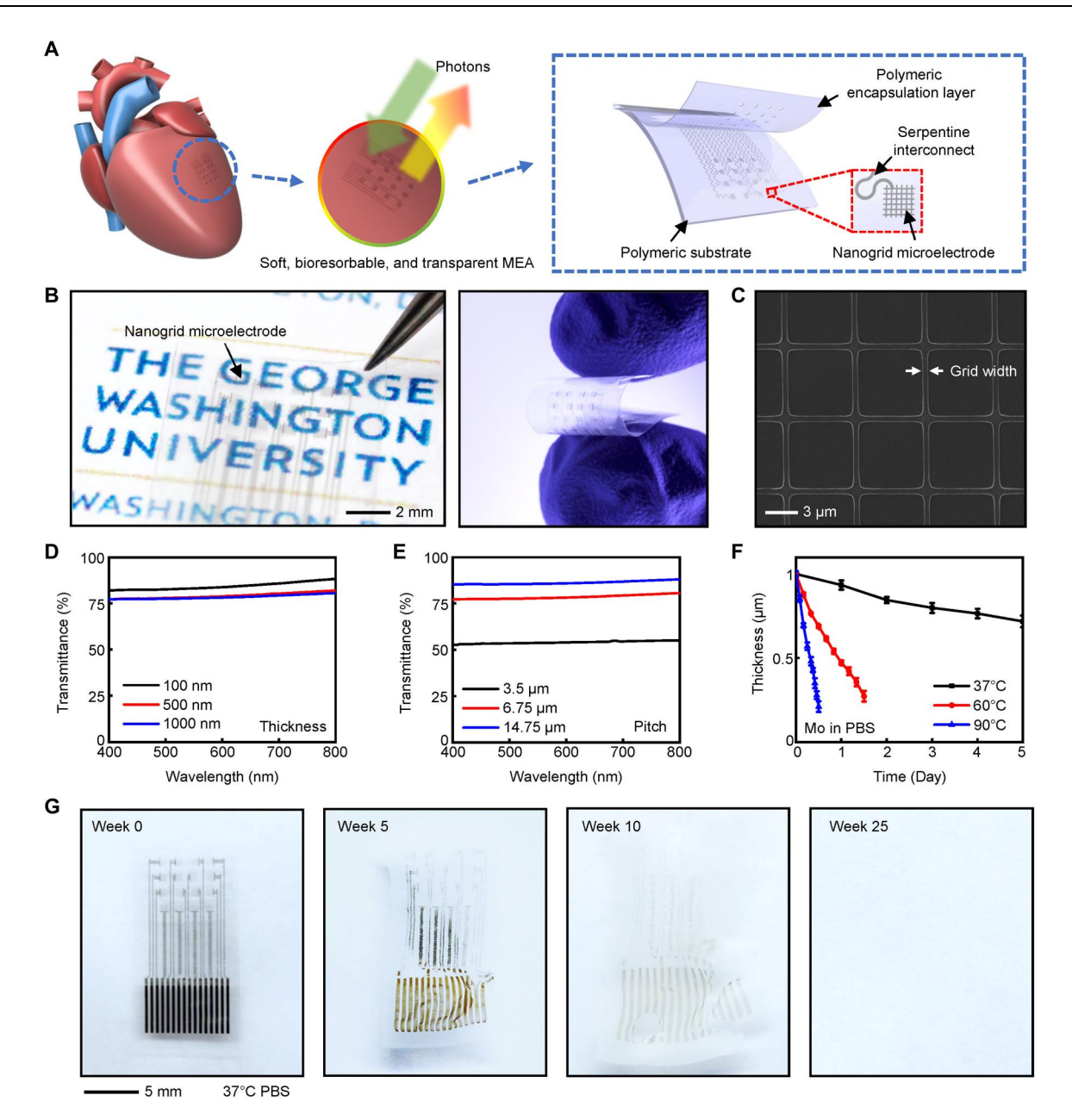


Fig. 1. Soft, bioresorbable, and transparent MEA for multimodal electrical and optical cardiac interrogation. (A) Schematic illustration of a MEA on a heart. The device consists of Mo nanogrid microelectrodes and interconnects, PLGA encapsulation, and substrate layers. (B) Optical images of the MEA to show transparency (left) and flexibility (right). (C) Scanning electron microscopy (SEM) image of the Mo nanogrid structure. Grid width, 500 nm; grid thickness, 1000 nm. (D) Transmission spectra of the Mo nanogrids (pitch, 6.75 μ m) at various thicknesses. (E) Transmission spectra of the Mo nanogrids (thickness, 1000 nm) at various pitch values. (F) Dissolution kinetics of 1000-nm-thick Mo layers in 1× PBS at 37°, 60°, and 90°C, evaluated as decreases in thicknesses. (G) Optical images of the MEA device at various dissolution stages in 1× PBS at 37°C.

37°C). The PLGA encapsulation and support layers dissolve by hydrolysis into its monomers, lactic acid, and glycolic acid (44). The results show that the MEA completely dissolves after 25 weeks. Scanning electron microscopy (SEM) measurements further illustrate the changes in surface morphologies at different soaking periods, revealing that the Mo nanogrids on the PLGA substrate gradually develop cracks due to the swelling of the substrate induced by PLGA dissolution, and most of the nanogrid patterns disappear from the MEA region after 5 weeks (fig. S3). High-

resolution transmission electron microscopy (HRTEM) and energy-dispersive x-ray spectroscopy (EDS) measurements (fig. S4) show that the lattice structures of Mo remain unchanged at initial stages of soaking (the interplanar spacing is 0.21, 0.21, and 0.22 nm at days 0, 1, and 2), while the oxygen content relative to Mo increases gradually in the devices.

Electrochemical impedance spectroscopy (EIS) and cyclic voltammetry (CV) measurements evaluate the recording and stimulation capability of the Mo nanogrid MEA. In general, a low

impedance at the electrode/electrolyte interface helps the microelectrodes suppress electrical noise and achieve high signal-to-noise ratios (SNRs) during recording. Figure 2A displays the impedance curves of Mo nanogrid microelectrodes at various thicknesses (grid width, 500 nm; pitch, 6.75 μm). The 1-kHz impedance decreases from 44.2 ± 2.8 to 23.9 ± 0.9 kilohms and 13.8 ± 0.8 kilohms as the Mo nanogrid thickness increases from 100 to 500 nm and 1000 nm, respectively. Figure 2B shows the impedance curves of the microelectrodes with various pitch values (grid width, 500 nm; thickness, 1000 nm). The 1-kHz impedance increases from 6.2 ± 0.4 to 13.8 ± 0.8 kilohms and 33.9 ± 1.5 kilohms as the pitch increases from 3.5 to 6.75 µm and 14.75 µm, respectively. Figure 2C depicts the linear dependence of 1-kHz impedance on the microelectrode sizes from 500 µm by 500 µm to 100 µm by 100 µm, indicating the presence of a capacitive interface between the Mo nanogrid microelectrode and the electrolyte solution. The phase angles of the microelectrode (-82.1° to -71.5°) at physiologically relevant low frequencies (10 Hz to 1 kHz) further confirm the capacitive electrode/electrolyte interface (Fig. 2D). Taking into account the balanced properties of optical transparency, electrochemical impedance, and device operational lifetime, the Mo nanogrid MEAs with a grid width of 500 nm, a pitch of 6.75 μm, and a thickness of 1000 nm are used in subsequent characterizations. Figure 2E compares the normalized 1-kHz impedance of the microelectrodes to state-of-the-art nonbioresorbable transparent microelectrode material candidates with comparable optical transparency (~80%) for electrophysiological studies, including indium tin oxide (ITO) (45), Au nanogrid (12), CNTs (9), graphene (46), and poly(3,4-ethylenedioxythiophene):polystyrene sulfonate (PEDOT:PSS) (10). The Mo nanogrid microelectrodes have one of the most competitive electrochemical performances. Figure 2F shows the CV curves of Mo nanogrid microelectrodes from -1.0 to -0.1 V at various scan rates from 20 to 200 mV/s. There is no observable distortion of the CV shape at a high scan rate of 200

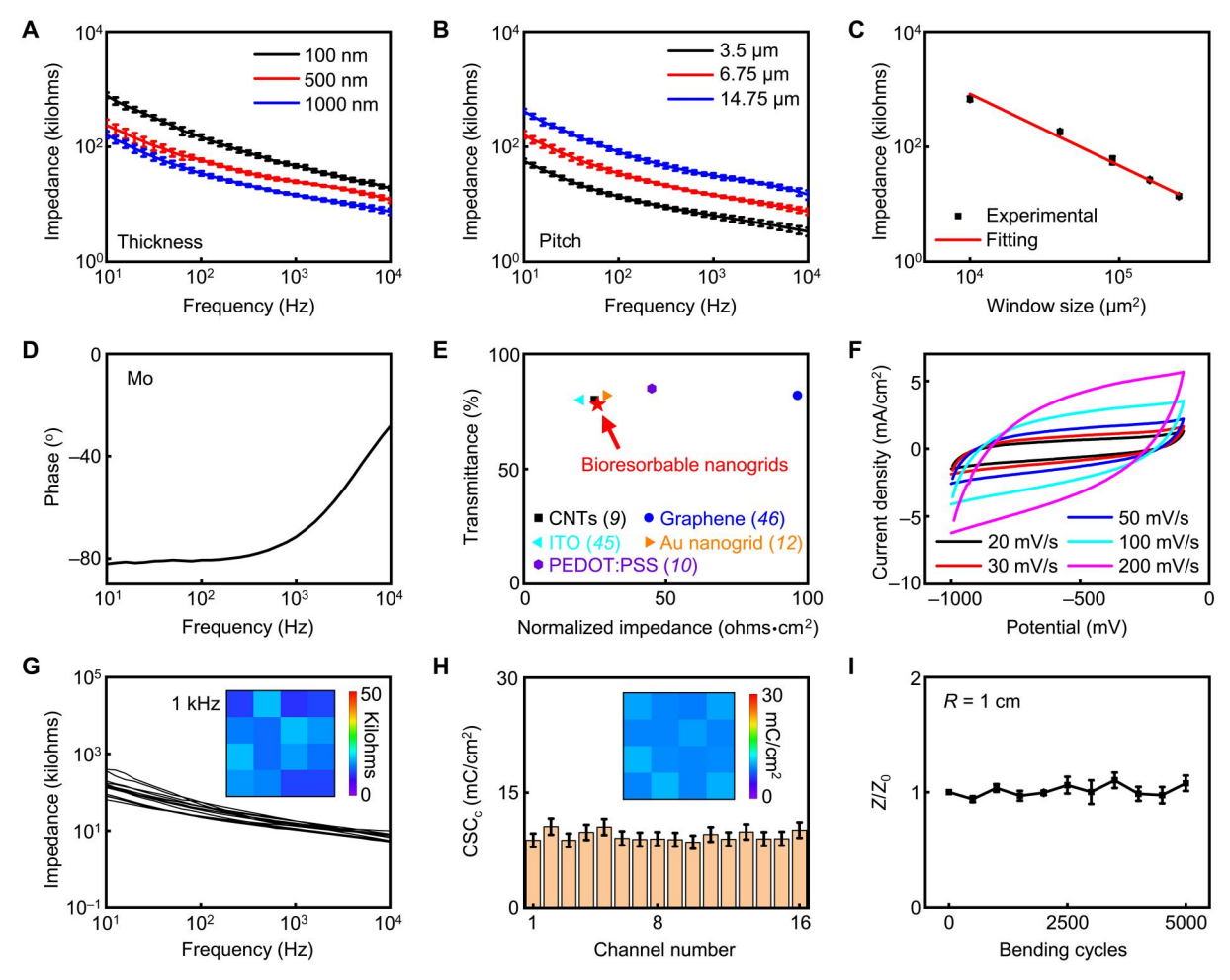


Fig. 2. Electrochemical characterization of Mo nanogrid microelectrodes and MEAs. (**A**) Impedance spectra of Mo nanogrid microelectrodes (pitch, 6.75 μm) at various thicknesses. (**B**) Impedance spectra of Mo nanogrid microelectrodes (thickness, 1000 nm) at various pitch values. (**C**) One-kilohertz impedance values of Mo nanogrid microelectrodes as a function of microelectrode sizes. (**D**) Phase plot of the Mo nanogrid microelectrode. (**E**) Normalized impedance versus transmittance comparison of different transparent microelectrode materials for electrophysiological studies where the Mo nanogrid microelectrode is the only bioresorbable one. (**F**) CV curves of a Mo nanogrid microelectrode at various scan rates. (**G**) Impedance spectra of all 16 Mo nanogrid microelectrodes in a MEA. Inset: One-kilohertz impedance color map of the microelectrodes relative to the actual microelectrode position in the MEA. (**H**) CSC_c histogram of 16 Mo nanogrid microelectrodes in a MEA at the scan rate of 50 mV/s. Inset: CSC_c color map of the microelectrodes relative to the actual microelectrode position in the MEA. (**I**) Impedance of a Mo nanogrid MEA as a function of bending cycles at a radius of 1 cm. *Z* and *Z*₀ represent the impedance value at a specific bending cycle and the initial impedance, respectively.

mV/s, indicating the excellent electrochemical stability of the microelectrodes at high current densities, a feature desired for cardiac pacing. Cathodic charge storage capacity (CSC_c) is an important metric to quantify the electrical stimulation performance of the microelectrodes. The average CSC_c value of the Mo nanogrid microelectrodes is 9.52 \pm 1.6 mC/cm², which is superior to many nonbioresorbable microelectrode materials, such as Pt (47, 48), Au (47, 48), titanium nitride (49), iridium oxide (49), graphene (9), CNTs (9), and ITO (table S1) (50).

A high degree of uniformity in the electrochemical performance of a MEA is critical for high-fidelity electrical cardiac mapping and pacing. Figure 2G presents the impedance responses of the 16 microelectrodes in a Mo nanogrid MEA, exhibiting an average 1-kHz impedance value of 14.2 \pm 2.7 kilohms. The inset impedance color map in Fig. 2G displays the spatial distribution of the 1-kHz impedance from the MEA to better visualize the uniform performance. Figure 2H demonstrates the highly uniform $\rm CSC_c$ values of all 16 microelectrode channels. Figure 2I shows that the MEAs maintain a stable electrochemical performance after 5000 bends against a small radius of 1 cm, suggesting the excellent mechanical compliance of the devices. The flexible mechanics is crucial to form a conformal contact with the curvilinear heart surfaces.

Recording 10-Hz sine waves at various physiologically related peak-to-peak amplitudes ranging from 100 μV to 20 mV in 1× PBS demonstrates the recording fidelity of the Mo nanogrid MEA (Fig. 3A and fig. S5). The 10-Hz impedance color map and histogram of the MEA are shown in fig. S6. No observable attenuation or distortion in the signal amplitude or morphology occurs, indicating the ability of the MEA to detect subtle electrophysiological signal

changes. The power spectral density (PSD) results in Fig. 3B provide detailed frequency domain information for the recorded signals. The large peak in the PSD curve corresponds to the 10-Hz input signal. The MEAs demonstrate highly uniform SNR and root mean square (RMS) noise, with an average SNR and RMS noise of 43.7 \pm 1.7 dB and 36.3 \pm 2.0 μV , respectively (Fig. 3, C and D). More SNR and RMS noise results from 64 other microelectrodes in four additional MEAs are available in fig. S7. Together, those measurements highlight the uniform performance for the microelectrodes both within the same MEA and across different MEAs in recording physiologically relevant signals.

Bioresorption behavior and its effect on the recording and stimulation properties of the MEA are critically important for temporary applications. Studies of the MEA performance changes during the resorption process are performed in 1× PBS at 37°C. Figure 3E presents average changes in the impedance (black line) and CSC_c (red line) from the microelectrodes over time. As expected, the impedance gradually increases, and CSCc gradually decreases because of the dissolution of Mo in PBS. We would like to note that the microelectrodes still exhibit moderate 1-kHz impedance (223.4 kilohms) and CSC_c (0.71 mC/cm²) on day 4. Fitting the EIS results before and after resorption to an equivalent circuit model (fig. S8) provides additional insights into the electrochemical behavior at the microelectrode-tissue interface. The model consists of solution resistance (R_s), the resistance of the oxide layer (R_{Oxide}), constant phase element (C_{PE}), charge-transfer resistance (R_{ct}) of the electrochemical corrosion process, and Warburg impedance $(Z_{\rm w})$ for ion diffusion. A parallel capacitance (C_L) and resistance (R_L) are added in series to fit the impedance data at high-frequency

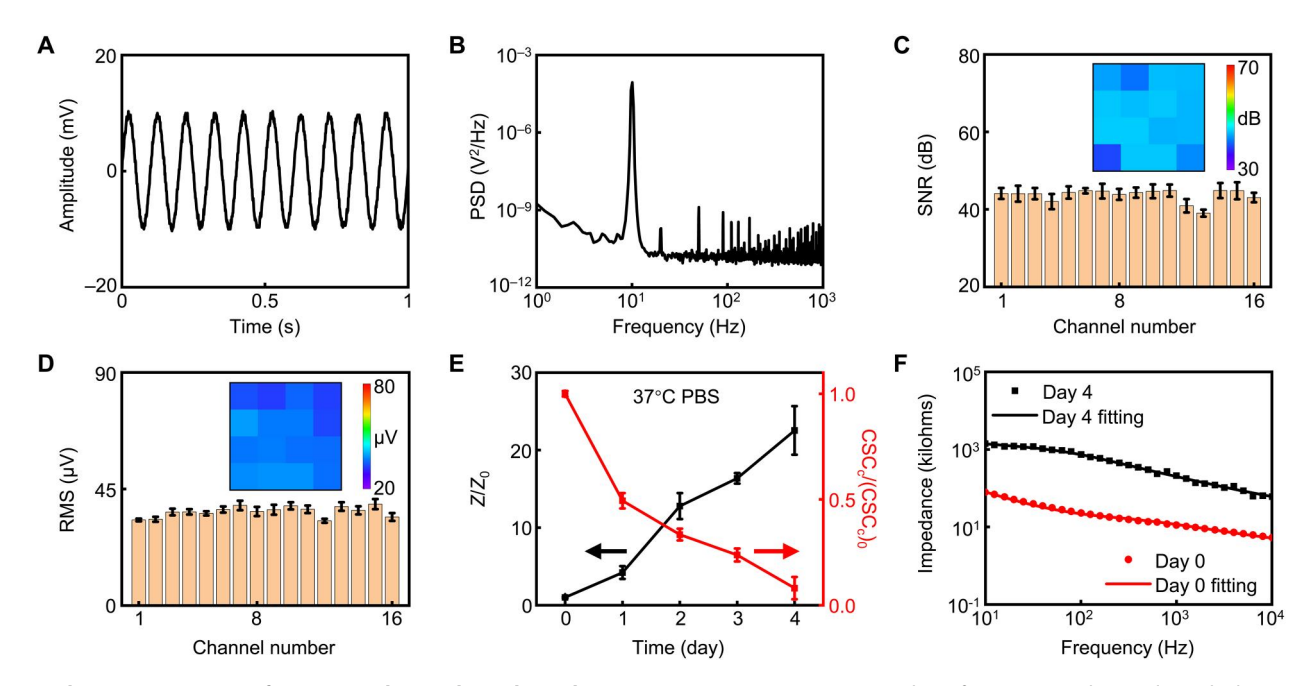


Fig. 3. Benchtop measurements of Mo nanogrid microelectrodes and MEAs. (A) Representative output recording of a Mo nanogrid microelectrode during a 10-Hz, 20-mV peak-to-peak amplitude sine wave input delivered by a Pt electrode in PBS. (B) Representative PSD curve of the recorded signals in (A). (C) Histogram of calculated SNRs of 16 microelectrodes in a MEA. Inset: SNR color map of the microelectrodes relative to the actual microelectrode position in the MEA. (D) Histogram of calculated RMS noises of 16 microelectrodes in a MEA. Inset: RMS noise color map of the microelectrodes relative to the actual microelectrode position in the MEA. (E) Changes in impedance (black line) and CSC_c (red line) during dissolution in PBS at 37°C. Z and CSC_c represent the impedance and CSC_c value at a specific day, while Z_0 and CSC_c represent the initial impedance and CSC_c respectively. (F) Impedance curves and equivalent circuit model fittings of the MEAs at different dissolution stages on days 0 and 4, respectively.

domains due to the charge transfer process at the exterior surface of the microelectrode (51, 52). The experimental data from days 0 and 4 closely match the fitting model (Fig. 3F). Table S2 summarizes the fitting results. The increased $R_{\rm s}$, $R_{\rm L}$, $R_{\rm Oxide}$, $R_{\rm ct}$, and $Z_{\rm w}$ on day 4 suggest a rise in the overall resistance and ion diffusion pathways due to the Mo corrosion and dissolution at the electrode/electrolyte interface. Furthermore, $C_{\rm PE}$ is defined as $\frac{1}{Y_0(j\omega)^n}$, where Y_0 , j, ω , and n values represent the magnitude of $C_{\rm PE}$, unit imaginary number, angular frequency, and a constant that determines the nature of the capacitance, respectively (53). The decrease in the n value (n value ranges from 0 to 1, where n=1 represents an ideal capacitor and n=0 represents a pure resistor) indicates a shift in the electrochemical behavior of the electrode surface from capacitive to more resistive, which aligns with the increase in overall resistance and correlates with the decrease in $C_{\rm L}$.

Ex vivo demonstration in various cardiac models

Ex vivo experiments on rat hearts and human ventricular tissue slices demonstrate the functionalities and capabilities of the bioresorbable and transparent Mo nanogrid MEA for simultaneous, colocalized, electrical, and optical interrogation of cardiac electromechanical function. Figure 4A (top) illustrates the experimental setup for interfacing with rat hearts, where the MEA is attached to the left ventricle of a Langendorff-perfused heart for electrogram (EG) mapping, synchronized with a two-complementary metal-oxide semiconductor (CMOS) camera-based optical mapping system for concurrent transmembrane potential (V_m) and intracellular calcium (Ca²⁺) fluorescence mapping. The high transparency (between 77.6% and 80.3%) of the device from 520 to 780 nm enables efficient passage of the excitation and emission photons from the light source and voltage- and calcium-sensitive dyes (RH237 and Rhod-2 AM), allowing for multiparametric high-content assessment of cardiac tissue electrophysiological function from the same field of view (Fig. 4A, bottom). Figure 4B demonstrates the time-aligned ECG reference (blue line) recorded by Ag/AgCl electrodes, EG signals from all 16 MEA channels (black lines), and simultaneous and colocalized $V_{\rm m}$ (red lines) and Ca²⁺ (purple lines) fluorescence signals from the area beneath each transparent microelectrode during sinus rhythm. The average heart rate recorded by the Mo nanogrid MEA EG results is 176 ± 1.1 beats per minute (BPM), which is consistent with that (176 \pm 1.6 BPM) from the far-field ECG. No observable transients or oscillations occur in the recorded local field potentials (or spikes) from all MEA-recorded EG traces, suggesting negligible light-induced artifacts during the light-emitting diode (LED) excitation illumination (520 nm; irradiance, 4.5 mW/mm²) and fluorescence emission, consistent with the previous report (12). Here, the Mo nanogrid MEA collects cardiac wave propagation profiles from the epicardium, while the voltage fluorescence signals present the dynamic $V_{\rm m}$ of cardiomyocytes located approximately 0.5 to 1 mm in depth of the cardiac tissue. The inward calcium channels open during the membrane depolarization, allowing an influx of calcium ions into the cell. These calcium ions trigger the opening of the calcium release channel of the sarcoplasmic reticulum membrane, resulting in the massive release of calcium into the cytosol to activate mechanical contractions. This process of calcium-induced calcium release causes a time delay between membrane depolarization and intracellular calcium transient, which is critically important in synchronizing cardiac contraction. The calculated EG-Ca²⁺ activation delay (5.49 ± 0.26)

ms) matches well with the optical $V_{\rm m}$ -Ca²⁺ activation delay (5.33) ± 0.87 ms), demonstrating the high-fidelity recording performance of the MEA to investigate cardiac excitation-contraction coupling. Figure 4C displays the electrical activation map (middle) constructed from the depolarization (activation) times of the MEA-recorded EG signals, optical $V_{\rm m}$ (left), and Ca^{2+} (right) activation maps. All three maps are synchronized, with white squares highlighting the region covered by the transparent MEA. The total epicardial activation time obtained from the same region via the MEA and optical mapping is 1.6 and 1.5 ms, respectively. Here, the extracted apparent conduction velocity by the MEA is 257.7 cm/s during sinus rhythm. Apparent conductivity characterizes the propagation speed of depolarization waves from the epicardial surface, while the electrical waves originate from the sinoatrial node (e.g., sinus rhythm) and spread out through a complex three-dimensional architecture. The comparison between the EG, $V_{\rm m}$, and ${\rm Ca}^{2+}$ activation maps visualizes the spatial-temporal distribution of the EG-Ca²⁺ and V_m-Ca²⁺ activation delays described previously. The high correlation between the EG and optical $V_{\rm m}$ maps of the same region further emphasizes the high-fidelity mapping capabilities of the MEA. The above results demonstrate that the Mo nanogrid MEA enables seamless interrogation of three notable cardiac parameters (EG, $V_{\rm m}$, and Ca²⁺) via different imaging modalities to accurately detect cardiac wave propagation patterns, as well as electrical and mechanical dynamics.

Moreover, the Mo nanogrid MEA is capable of electrical pacing using one or more microelectrodes in the array to modulate cardiac activity, treat abnormalities in the electromechanical properties, and simultaneously assess the pacing effects by electrical mapping using the rest microelectrodes. Figure 4D demonstrates the EG, $V_{\rm m}$, and Ca²⁺ activation maps upon electrical stimulation (400 BPM) delivered from the top right corner microelectrode in the MEA. Here, the extracted longitudinal (transverse) conduction velocities from the MEA and optical mapping during pacing are 56.9 (32.4) and 57.6 (32.6) cm/s, respectively. The three activation maps and their strong correlations (i) indicate successful capture of the heart rhythm, as the cardiac activation now originates from the pacing site and chronologically propagates throughout the heart surface in an anisotropic way and (ii) highlight the synchronized cardiac pacing and high-fidelity mapping capabilities of the MEA. Figure 4E summarizes representative QRS complexes recorded by the Mo nanogrid MEA across a relevant therapeutic period (days 0 to 3) during sinus rhythm. As the device gradually dissolves in PBS, the amplitude of the recorded QRS complexes becomes smaller. Gradually, the calculated SNR decreases from 35.7 \pm 0.74 to 33.9 ± 0.68 dB, 30.2 ± 0.71 dB, and 26.8 ± 0.80 dB after 0, 1, 2, and 3 days in PBS, respectively.

Ex vivo demonstration on human ventricular slices (thickness, ~400 $\mu m)$ validates the practical feasibility of the MEA in potential clinical scenarios (Fig. 4F). The high optical transparency of the MEA enables clear visualization of the underneath human cardiac tissue to facilitate device positioning. In Fig. 4G, the strong correlation between MEA EG and the optical $V_{\rm m}$ activation maps demonstrates the successful mapping of the electrical activities of human ventricular slices. The calculated conduction velocities in the tissue slice preparation from the MEA and optical mapping during pacing are both 24.5 cm/s, respectively. Together, the ex vivo results reveal that the bioresorbable and transparent Mo nanogrid MEAs are

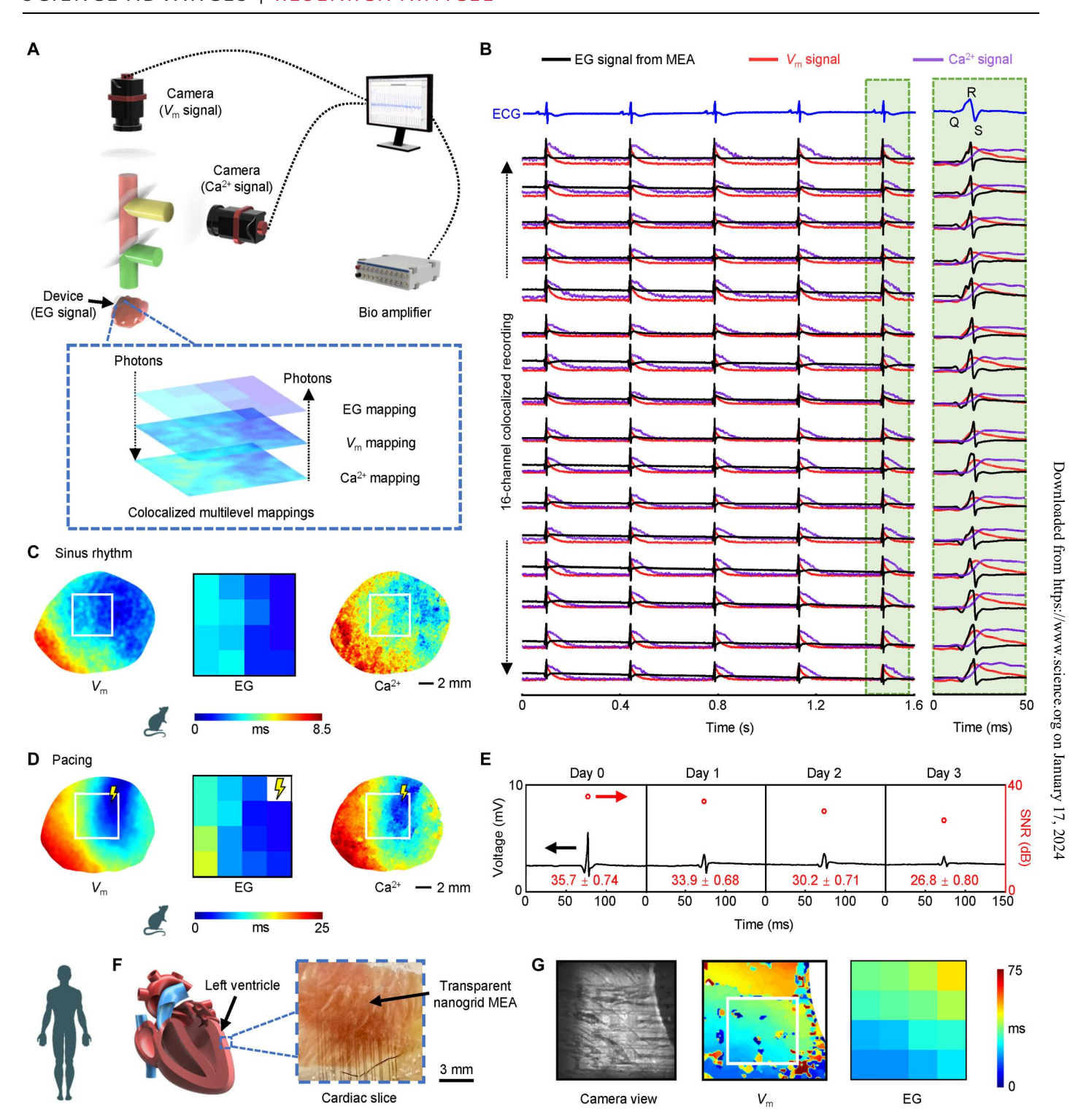


Fig. 4. Ex vivo demonstration of the MEA for simultaneous colocalized electrical/optical interrogation of rat hearts and human ventricular slices. (A) Top: Schematic illustration of EG mapping (from the MEAs) and optical dual mapping (V_m and Ca^{2+}) setup. Bottom: Schematic illustration of simultaneous multilevel and multiparametric mapping in the same field of view. (B) Synchronous and colocalized EG, V_m , and Ca^{2+} traces recorded from different cardiac tissue regions beneath the transparent microelectrodes of the MEA during sinus rhythm. Green box: Zoomed-in view of three overlapping traces at each microelectrode of the MEA. (C) Concurrent V_m (left), EG (middle), and Ca^{2+} (right) activation maps during sinus rhythm. The white square represents the region covered by the transparent MEA. (D) Concurrent V_m (left), EG (middle), and Ca^{2+} (right) activation maps during MEA pacing. The pacing site is marked with yellow lightning bolts. (E) QRS complexes (black line) recorded by the MEAs at various dissolution stages in PBS at 37°C and correlated SNRs (red symbol). The QRS complexes are recorded from the same rat heart. (F) Left: Schematic illustration of the region where the human ventricular slices are collected. Right: Optical image of the MEA on a human cardiac slice to show transparency. (G) Camera view of the MEA on a human cardiac slice (left), V_m (middle), and EG (right) activation maps.

suitable for cross-platform cardiac electro/optophysiological applications ranging from rat hearts to human cardiac tissue slices.

In vivo demonstration of AV block management

In vivo, open-chest studies illustrate the performance of the Mo nanogrid MEAs in mapping and modulating the dynamic physiology of blood-perfused beating hearts. Figure 5A displays the experimental setup, where the MEA is placed on the left ventricle of an actively contracting rat heart. Figure 5B shows the cardiac wave propagation recorded by the MEA during sinus rhythm with an average heart rate of 378 ± 1.9 BPM, which is faster than the ex vivo rat heart excitation in Fig. 4C (177 \pm 1.1 BPM) due to autonomic innervation of the cardiac conduction system and various circulating humoral factors and metabolic substrates absent from a Langendorff perfused heart. Figure 5C and movies presented in the Supplementary Materials (movie S1 and S2) show that the MEA can concurrently manipulate and map the cardiac wave propagation patterns from an in situ heart by unipolar pacing at 400 BPM (voltage, 2 V; pulse width, 2 ms) at different locations. In the unipolar pacing mode, one Mo nanogrid microelectrode functions as the cathode, and a remote Pt electrode works as the anode. Clinically, both unipolar and bipolar configurations are used in therapeutic pacing, while bipolar pacing is generally preferred because it requires a lower pacing threshold that consumes less energy and minimizes pectoral muscle stimulation, which may occur during unipolar pacing due to current return to the pulse generator (54–56). Figure 5D illustrates the control and capture of the cardiac excitation wave activation and propagation by bipolar pacing using the Mo nanogrid MEA (voltage, 1.5 V; pulse width, 2 ms), where two nearby microelectrodes in the MEA serve as the anode and cathode.

Cardiac pacing is frequently used in the clinic to treat abnormal heart rhythms such as bradycardia, where the heartbeat is too slow to support the normal cardiovascular circulation (57, 58). Bradycardia can be caused by several reasons, such as congenital heart defects, postsurgical complications, TAVR, and AV block (57). AV block is an interruption in transmitting an impulse between the atria and the ventricles, resulting in the desynchronization of atrial and ventricular excitation and a reduced heart rate. Ventricular pacing is widely used to resynchronize ventricular and atrial contractions, restore normal heart rate and hemodynamics, and treat patients with AV block. Figure 5E demonstrates the detection and treatment of AV block with the Mo nanogrid MEA. The ECG signals show a 3:1 AV block with ventricular contractions occurring at the slow rate of 58 BPM, indicated by three consecutive P waves and only one QRS complex (58). The ECG traces and EG signals recorded by the 14 sensing microelectrodes exhibit clear high-amplitude and wide QRS complexes during bipolar pacing at 400 BPM, showing the successful rhythm capture of the beating heart. Different shapes of the EG traces during bipolar pacing represent different depolarization and repolarization responses of the local cardiac tissue beneath each microelectrode. The MEA maps different propagation patterns of the depolarization waves during AV block and pacing (fig. S9). The measured longitudinal and transverse conduction velocities of the depolarization wave during MEA-initiated bipolar pacing are 51.1 and 31.6 cm/s, respectively. When the pacing stops, the AV block resumes with the rate of ventricular contractions of 55 BPM, indicating that the device pacing is responsible for and required to maintain a normal heart rate. Figure 5F

summarizes the QRS complexes recorded by the Mo nanogrid MEAs on days 0 to 4 during sinus rhythm. The dissolution is completed in PBS, while the EG mapping is performed on the bloodperfused beating hearts during in vivo open-chest measurements. The decline in SNR from the in vivo recording results is consistent with the ex vivo recording results in Fig. 4E, resulting from the increased impedance during the MEA dissolution process in PBS. Note that the different features of the QRS complexes during sinus rhythm in Figs. 5F and 4E are normal and mainly determined by the locations of the microelectrodes on the heart and cardiac physiology because the EG results only represent electrical excitation of a local area under and near the microelectrodes instead of the whole heart in far-field ECG results. Similar differences exist in EGs from nonbioresorbable Au microelectrodes (fig. S10) and are reported by other groups (59-61). These results demonstrate that the bioresorbable and transparent Mo nanogrid MEAs enable in vivo arrhythmia detection, monitoring, and treatment in the beating hearts for cardiac rhythm management (movie S3).

In vivo bioresorbability and biocompatibility

The in vivo bioresorption process and biocompatibility of the Mo nanogrid MEAs are investigated by performing visual, functional, histological, and serological evaluations at different time points after MEA implantation. Rats of both sexes are randomly assigned into three groups (n = 3 animals per group): The control group does not receive any artificial interventions. The MEA group undergoes the open-chest surgery and MEA implantation via suture stitching of the device onto the left ventricular epicardium. The sham group undergoes the same open-chest surgery and suture stitching but without MEA implantation. The sham group at 2 weeks after sham surgeries and the MEA group at 2 and 6 weeks after implantation surgeries are examined for visual traces of the MEA bioresorption. Figure 6A displays the optical images of the hearts in situ (square box) and after explantation (circular box). The optical image at week 0 shows that the MEA is mechanically robust to survive the surgical handling during implantation. At week 2, the MEA partially dissolves with visible Mo pattern residues. At week 6, the MEA completely disappears from the heart surface at the implantation region. Fibrotic tissues and nonbioresorbable proline sutures exist in all rats of the MEA and sham groups, resulting in tissue damage during surgeries (e.g., stitching the epicardium) (62).

Figure 6B demonstrates the representative histology images of Masson's trichrome staining of cardiac tissues undergoing MEA implantation surgeries, where the red color represents muscle fiber (i.e., cardiomyocytes) staining, the blue color represents collagen (i.e., fibrotic area) staining, and the white color represents interstitial space. The green triangle indicates the epicardial side. Fibrosis occurs over the epicardial region where the MEAs are implanted. The normal myocardium comprises several major cell types (e.g., cardiomyocytes, fibroblasts, neurons, endothelial cells, etc.), forming a complex three-dimensional architectural network including the collagen scaffold and interstitial space. Pathophysiological conditions (e.g., cardiac injury, infarction, heart failure, and infections) are characterized by myocardial fibrosis and interstitial space expansion, which, in turn, increase ventricular stiffness and lead to decreased electrical synchronization and mechanical contractility (63, 64). Figure 6C exhibits the quantification of the histology examination, where the percentage volume of cardiomyocytes,

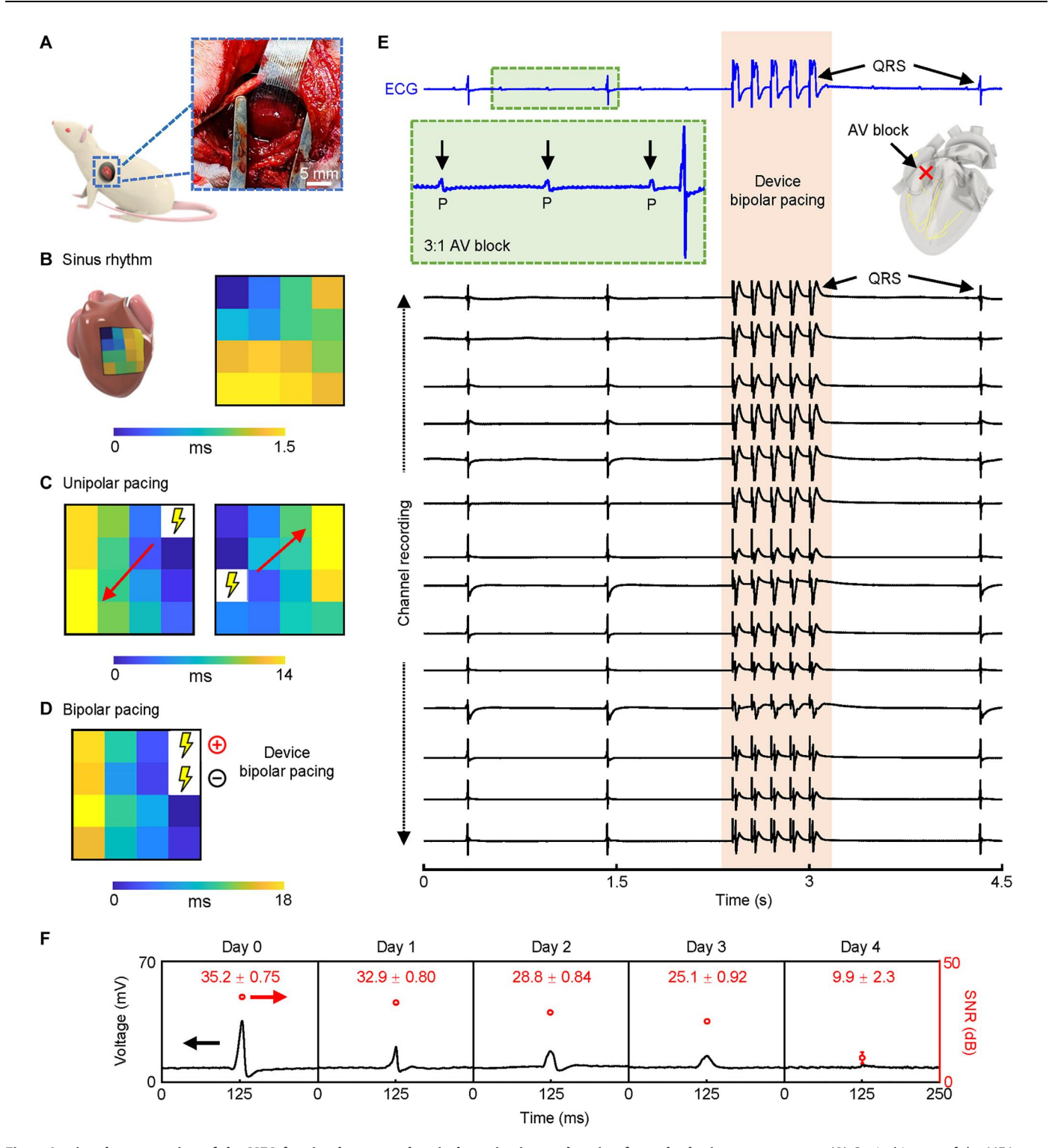


Fig. 5. In vivo demonstration of the MEA for simultaneous electrical monitoring and pacing for arrhythmias management. (A) Optical image of the MEA contacting the left ventricle of a blood-perfused rat heart to show transparency and flexibility. (B) Left: Schematic illustration of the electrical mapping location of the MEA on a rat heart (front-lateral side of the left ventricle). Right: Electrical activation map generated by the MEA during sinus rhythm. (C) Electrical activation maps from the MEA during unipolar pacing at different sites. The pacing sites are marked with yellow lightning bolts. The red arrow represents the direction of cardiac wave propagation. (D) Electrical activation map from the MEA during bipolar pacing with two neighboring microelectrodes in the MEA. (E) Demonstration of MEA multichannel sensing and pacing capabilities for arrhythmia monitoring and treatment. Orange box, simultaneous EG recording and bipolar pacing from the MEA during 3:1 AV block; green box, zoomed in view of the 3:1 AV block recorded by far-field ECG. The location of AV block (cartoon). (F) QRS complexes (black line) recorded by the bioresorbable MEAs at various dissolution stages in PBS at 37°C and correlated SNRs (red symbol). The QRS complexes are recorded from the same rat heart.

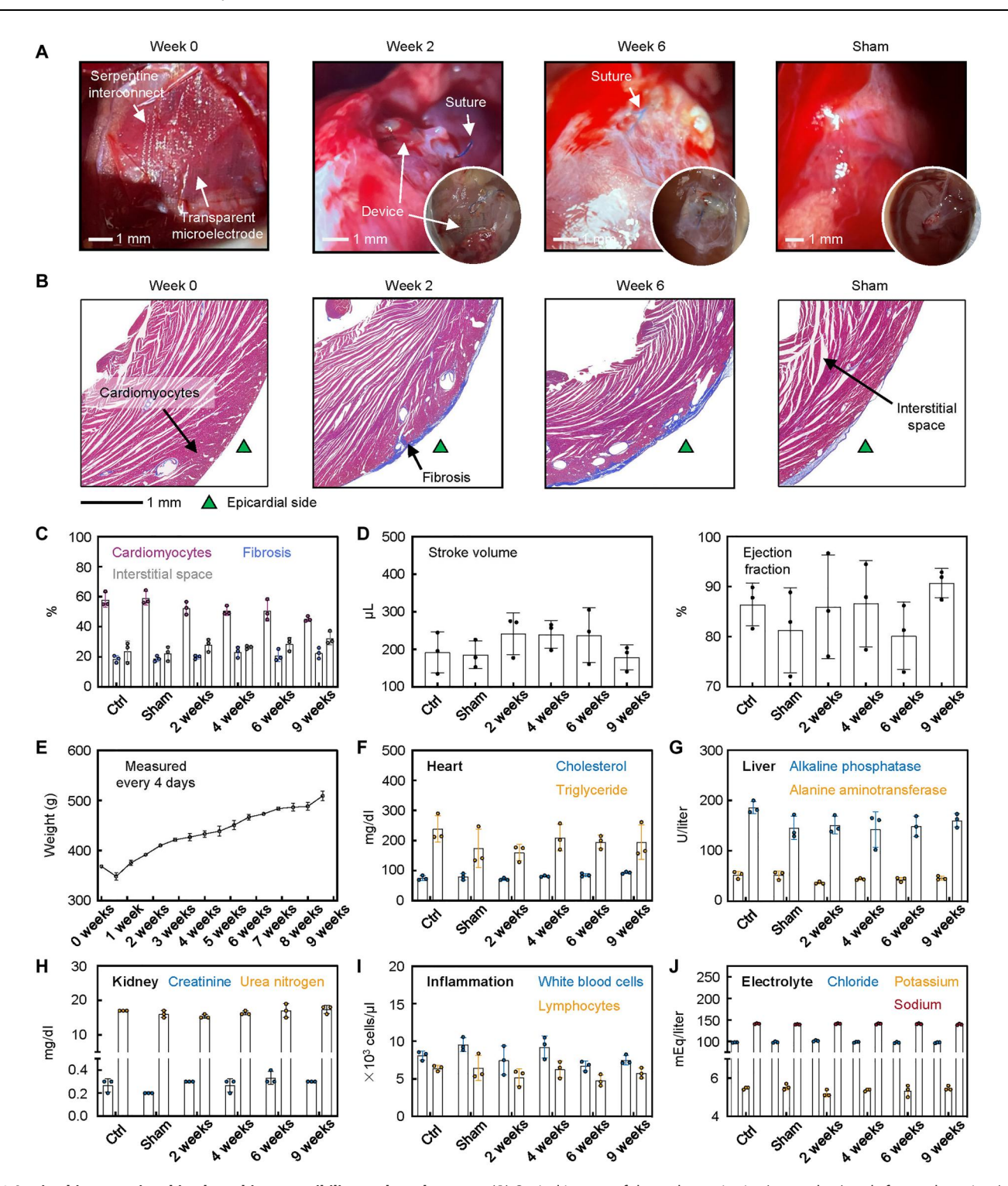


Fig. 6. In vivo bioresorption, histology, biocompatibility, and serology test. (**A**) Optical images of the rat hearts in situ (square box) and after explantation (circular box). (**B**) Representative histology images of Masson's trichrome staining of cardiac tissues. Red, cardiomyocyte staining; blue, fibrosis staining; white, interstitial space staining. Devices are stitched over the epicardium (the green triangle indicates the epicardial side). (**C**) Quantified volume percentage of the cardiomyocytes, fibrosis, and interstitial space in (B). No statistically significant difference is found among different groups. (**D**) Transthoracic echocardiogram test on the stroke volume and ejection function of the heart at different time points after implantation. No statistically significant difference is found. (**E**) Weight measurement of the animals at different time points after implantation. A normal weight loss is observed immediately after the surgery and is followed by a gradual weight gain resulting from a natural increase in age. Serology test of biomarkers for the evaluation of the function of heart (**F**), liver (**G**), and kidney (**H**) and the level of inflammation (**I**) and electrolyte (**J**). No statistically significant difference is found among different groups. Data are presented with error bars as means \pm S.D. The statistical comparison among different groups is calculated with a nonparametric Kruskal-Wallis test in conjunction with Dunn's multiple comparisons tests at a significance level of P < 0.05. P

fibrosis, and interstitial space reveals no statistically significant difference among all the groups (P < 0.05), which indicates negligible effects on the myocardial structures upon the MEA implantation and bioresorption. Figure 6D depicts the transthoracic echocardiogram test on the contractile function of the heart at different time points after implantation. Stroke volume and ejection fraction represent the volume and percentage of oxygen-rich blood pumped out from the left ventricle during each systolic contraction. A very low ejection fraction indicates impaired pumping action of the heart, which affects normal hemodynamics and is a hallmark of heart failure (65). Our results show no statistically significant difference in cardiac ejection fraction or volume among all the groups (P < 0.05), indicating no effect of our devices on normal contractility. The analysis of other hemodynamic parameters (i.e., diastolic and systolic volume and diameter, cardiac output, and fractional shortening) shows similar normal results among different groups (fig. S11), indicating negligible effects on the mechanical function of the heart after the MEA implantation. Figure 6E demonstrates the weights of the animals at different time points after implantation. An anticipated weight loss immediately after surgery is followed by a normal, gradual weight gain with age.

The serology tests (i.e., complete blood count and blood chemistry) provide a comprehensive understanding of the health status of animals at different stages after surgery (Fig. 6, F to J, and figs. S12 and S13). The blood levels of lipids, enzymes, metabolic wastes, immune cells, and electrolytes serve as indicators of organ-specific function and impairment, as well as foreign body response upon the MEA implantation and bioresorption. Specifically, high cholesterol and triglycerides are associated with a higher risk of stroke or heart attack (66). Alkaline phosphatase reflects the function of liver to form and release bile, while elevated alanine aminotransferase indicates potential hepatocellular injury (67). High keratinize and urea nitrogen levels indicate potential impaired renal function to excrete waste products and toxins (68). White blood cells (including lymphocytes, eosinophils, monocytes, and basophils) play critical roles in inflammatory reactions. Electrolytes can affect heart rate and rhythm, stabilize blood pressure, and support nerve and muscle function. The results (Fig. 6, F to J, and figs. S12 and S13) show no statistically significant difference in organ function or physiological status among all the groups. The similar levels of average counts of red blood cells, white blood cells, monocytes, and lymphocytes indicate no notable inflammation in sham and MEA groups. The stable level of electrolytes shows the overall good health of animals in different groups. Together, those results suggest the harmless in vivo bioresorption of the Mo nanogrid MEA without abnormalities in the normal physiology of animals.

DISCUSSION

The materials, device designs, and fabrication approaches reported here yield a fully bioresorbable and transparent MEA platform that (i) provides mechanically compliant bidirectional electrical mapping and pacing over clinically relevant temporary time scales and (ii) enables colocalized cross-talk—free multiparametric monitoring of cardiac behaviors. The MEA is lightweight, thin, and highly transparent; has excellent mechanical flexibility and superior and uniform electrochemical performances; and complements those of the traditional nonbioresorbable MEAs. Studies on small animals and human hearts highlight the function of the MEA for

spatiotemporal mapping of a list of critical cardiac parameters and demand-based site-specific unipolar and bipolar pacing to treat AV block. Systematic bioresorption and biocompatibility evaluations demonstrate that the entire MEA has excellent biocompatibility and can fully dissolve from the implantation region in living animal models after 6 weeks, eliminating the need for secondary surgical procedures for device extraction. These concepts establish unique approaches in bioresorbable device technologies for fundamental studies of the pathophysiology of heart disease, with additional possible utility in developing effective clinical therapies, guiding surgical procedures, and monitoring postoperative recovery. Future opportunities include the development of wireless systems for power harvesting, control, and data communications; algorithms for automated closed-loop operations; and optimization of the operational lifetimes to treat various forms of temporary heart conditions in clinical scenarios.

MATERIALS AND METHODS

Fabrication of Mo nanogrid MEA

The fabrication of Mo nanogrid MEA started with laminating an aluminum (Al) foil on a handling glass slide with polyimide tapes (Advanced Polymer Tape Inc.) on the edges. Oxygen plasma (50 W, 180 mtorr, and 3 min) treated the prepared Al foil/glass slide before use. Poly(methyl methacrylate) (PMMA) resist (MicroChem) was spin-coated on the Al foil/glass slide and baked at 95°C for 450 s. Electron beam evaporation deposited an 8-nm-thick Cr layer onto the PMMA layer to serve as a conductive layer for EBL. EBL defined the nanogrid MEA structure via a beam current of 1 nA. Sputter deposition prepared a 1000-nm-thick Mo on the MEA followed by a lift-off process in acetone. Photolithography with AZ nLOF 2070 photoresist (Integrated Micro Materials) defined the interconnects and bonding pad structures of the MEA. A second sputter deposition of Mo (1000 nm thick) followed by lift-off in acetone completed the fabrication of the interconnects. Afterward, a 25 weight % (wt%) PLGA (65:35; Sigma-Aldrich Inc.)/ethyl acetate (anhydrous, 99.8%; Sigma-Aldrich Inc.) solution was spin-coated onto the sample, followed by baking at 60°C for 5 hours and 110°C for 2 hours. Then, the film was delaminated from the glass slide by gently peeling off the polyimide tapes on the edges without deforming the film. Last, immersing in hydrochloric acid (37%; High Purity Products) released the transparent Mo nanogrid MEA from the Al foil.

To prepare the encapsulation PLGA layer, a 15 wt% PLGA/ethyl acetate solution was spin-coated on a soft lithography—defined polydimethylsiloxane (PDMS) stamp, followed by baking at 60°C for 2 hours. After cooling down, the PLGA encapsulation layer was gently peeled off from the PDMS stamp. The prepared PLGA encapsulation layer and Mo nanogrid MEA were then aligned together under a microscope, baked at 50°C for 2 min, and bonded in ethyl acetate vapor for 3 hours. Last, the device was baked at 50°C for another 5 min to improve the adhesion.

Optical, SEM, and mechanical measurements

A spectrophotometer (V-770 UV-visible/NIR; Jasco Inc.) measured the transmission spectra of the Mo nanogrid MEAs. SEM (PIONEER EBL; Raith Inc.) investigated the morphology of the nanogrids. A FEI Talos F200X scanning transmission electron microscope performed HRTEM and EDS measurements. A motorized

test stand (ESM 1500; Mark-10) performed mechanical bending tests, in which the electrochemical performance was measured separately after a specific cycle of bending (fig. S14).

Electrochemical measurements

EIS and CV measurements were conducted by a Gamry potentiostat (Reference 600+; Gamry Instruments Inc.) via a three-electrode configuration in $1\times$ PBS (fig. S15). In the configuration, an Ag/AgCl electrode, a Pt electrode, and the Mo nanogrid microelectrode served as the reference, counter, and working electrodes, respectively. CSCc was calculated at a scan rate of 50 mV/s. For benchtop measurement, a data acquisition system (PowerLab 16/35; ADInstruments Inc.) delivered 10-Hz sine wave signals with peak-to-peak amplitudes from 100 μV to 20 mV via a Pt electrode in 1× PBS. The microelectrodes in the Mo nanogrid MEAs detected the signals. The recorded signals were processed using MATLAB to obtain SNR and RMS noise.

Animals

All animal procedures were performed according to protocols approved by the Institutional Animal Care and Use Committee of The George Washington University and Northwestern University and in conformance with the *Guide for the Care and Use of Laboratory Animals* published by the National Institutes of Health. Sprague-Dawley rats (male and female; Hilltop Lab Animals) at 10 to 17 weeks old were used.

Animal groups

Animals of both sexes were randomly assigned in three groups. Animals in the control group (n = 3) received no artificial procedures or interventions. Animals in the device group (n = 3) received the open-chest surgery and device implantation (including suture stitching of the device onto the epicardium). Animals in the sham group (n = 3) received the open-chest surgery and suture stitching without device implantation. We used nonresorbable sutures to indicate the location of devices after resorption.

Device implantation surgery and weight monitoring

The rat was anesthetized using isoflurane (1 to 3%). Once sedated, an intraperitoneal injection of buprenorphine (0.5 to 1.0 mg/kg) analgesia was administered. The rat was then placed supine on the intubation stage, and intubation was performed using the standard technique (62). Once intubated, the rat was placed on pressure-controlled ventilation in the right lateral decubitus position. Animal ventilation was provided by the VentElite small animal ventilator (Harvard Apparatus, Holliston, MA). ECG leads were connected for intraoperative cardiac monitoring (lead II configuration). The left lateral chest was shaved and prepped using a sterile skin prep. The rat was then covered with a sterile drape, exposing the surgical site. The chest was palpated to identify the intercostal space where the point of maximum impulse could best be palpated. Scissors were used to make a curvilinear incision through the skin and subcutaneous tissue across the chest wall over the intercostal space. Metzenbaum scissors were then used to dissect through the chest wall muscles and into the thoracic cavity with care taken not to injure the lung. A rib spreader then opened the intercostal space. A cotton swab gently retracted the lung to expose the heart. Another cotton swab gently removed the pericardium. The MEA was then laid over the left ventricle. Two 6.0 Prolene simple

interrupted stitches (nonbioresorbable) secured the MEA to the heart. The cotton swab retracting the lung was carefully removed from the chest, and the lung was placed back over the heart on top of the device. The rib spreader was then removed, and the chest wall was closed with three single interrupted stitches using 4.0 polydioxanone (PDS) sutures. The muscle layer was also closed using PDS with single interrupted sutures. The skin incision was closed with 4.0 nylon sutures in a running fashion. Anesthesia was then stopped, and the rat was allowed to recover on the ventilator until the point of self extubation. Appropriate postoperative monitoring and care were provided following surgery. The intraperitoneal dose of buprenorphine (0.5 to 1.0 mg/kg) analgesia was administered once every 12 hours for 48 hours following surgery. Animals (n=3) were weighed every 4 days to monitor the weight after surgery.

Echocardiogram

Echocardiogram was performed to evaluate the mechanical function of the left ventricle of the heart. There were n = 3 Sprague-Dawley rats for each group (i.e., control, MEA implantation, and sham). Control group did not receive any surgery, and echocardiogram was performed directly. Echocardiogram of the MEA implantation group was performed at 2, 4, 6, and 9 weeks after the implantation surgery. Echocardiogram of the sham group was performed at 2 weeks after the sham surgery. Rats were anesthetized by inhalation of 1 to 3% isoflurane vapors at oxygen flow of 2 ml/min before and during the echocardiogram imaging with an EZ anesthesia machine (EZ Systems Inc., EZ-SA 800). Rats were transferred to the imaging stage after confirmation of loss of consciousness. Paws were affixed to the ECG electrodes (of the imaging stage) with electrode gel and tape to monitor the heart rate throughout echocardiogram imaging. Heart rate was maintained at 250 to 300 BPM. The left lateral chest was shaved, and ultrasound gel (Aquasonic) was applied to the skin. M-mode echocardiography of the left ventricle was performed using the Vevo 3100 system (VisualSonics/Fujifilm). The data were analyzed with VevoLAB2.1.0.

Lateral tail vein blood collection and serology test

There were n=3 Sprague-Dawley rats for each group (i.e., control, MEA implantation, and sham). Control group did not receive any surgery, and blood was collected directly. Blood from the MEA implantation group was collected at 2, 4, 6, and 9 weeks after the implantation surgery. Blood from the sham group was collected at 2 weeks after the sham surgery. Blood was stored in (i) serum tubes (1.3-ml micro tubes; Sarstedt Inc.) for serum complete chemistry tests and (ii) K3 EDTA tubes (1.3-ml micro tubes; Sarstedt Inc.) for complete blood count tests. A commercial company (Charles River Laboratories) conducted the assays.

Histology

There were n=3 Sprague-Dawley rats for each group (i.e., control, MEA implantation, and sham). Control group did not receive any surgery, and hearts were collected directly. Hearts from the MEA implantation group were collected at 2, 4, 6, and 9 weeks after implantation surgery. Hearts from the sham group were collected at 2 weeks after the sham surgery. Rats were euthanized using 5% isoflurane vapors at oxygen flow of 2 ml/min with an EZ anesthesia machine (EZ Systems Inc.) until loss of consciousness was confirmed via toe pinch. Hearts were excised and retrogradely perfused

via an aortic cannula with cardioplegic solution (110 mM NaCl, 16 mM KCl, 16 mM MgCl₂, 10 mM NaHCO₃, and 1.2 mM CaCl₂; 4°C) and then 10% neutral-buffered formalin. Hearts were transferred to a 70% ethanol solution after 24 hours of immersion (room temperature) in 10% neutral-buffered formalin. Cross sections of hearts were paraffin-embedded, sectioned, and stained with Masson's trichrome for identification of myocardium (red color), fibrosis (blue color), and interstitial space (white color). Tissue samples were imaged using an EVOS XL light microscope (Thermo Fisher Scientific). A custom MATLAB code was used to quantify the percent volume of cardiomyocytes, fibrosis, and interstitial space in the images (i.e., calculate the relative number of pixels per color in the selected region of interest).

Langendorff perfusion of the heart for ex vivo studies

Sprague-Dawley rats were anesthetized by ~3% isoflurane inhalation until no response to a toe pinch was confirmed. A cervical dislocation was performed followed by the thoracotomy. The heart was excised and retrogradely perfused via an aortic cannula in a constant-pressure (70 to 90 mmHg) mode. A modified Tyrode's solution [140 mM NaCl, 4.7 mM KCl, 1.05 mM MgCl₂, 1.3 mM CaCl₂, 11.1 mM glucose, and 10 mM Hepes (pH 7.4) at 37°C] bubbled with 100% $\rm O_2$ was used.

Ex vivo whole heart synchronized optical and electrical mapping

Optical mapping was performed as previously described (69). Blebbistatin (10 to 15 μM; Cayman Chemicals, catalog number 13186) was added into the perfusion solution to suppress cardiac contractions. For optical mapping of $V_{\rm m}$ and calcium transients, the voltage-sensitive dye RH237 [dye stock solution (1.25 mg/ml); Biotium, catalog number 61018] and calcium-sensitive dye Rhod-2 AM [dye stock solution (1 mg/ml); Thermo Fisher Scientific, catalog number R1244] were added via bolus injection through the cannula. Fluorescence dyes were perfused for 15 to 20 min (i.e., equilibration period) before optical mapping studies to allow tissue staining and the washout of extra dyes. Excitation light at 520 \pm 17-nm wavelength was used (LEX3-G Green LED System). $V_{\rm m}$ fluorescence was filtered by a 695-nm long-pass filter and calcium fluorescence was filtered by a 572 \pm 14–nm band-pass filter. Images of the front-lateral side of the left ventricle were captured at a speed of 2000 frames per second using two CMOS cameras (ULTIMA-L, SciMedia) with a 100×100 -pixel resolution (field of view, 15 mm by 15 mm). The MEA was placed on the front-lateral side of the left ventricle and connected to a data acquisition system (PowerLab 16/ 35, ADInstruments Inc.) with a sampling frequency of 20 kHz. Customized Pt bipolar electrodes or the Mo MEA were used to pace the heart from the left ventricle at rates higher than the intrinsic sinus rhythm of the heart. Electrical stimulation amplitude (i.e., pacing voltage) was set at 2× the pacing threshold.

Ex vivo cardiac slice synchronized optical and electrical mapping

Experiments with donor human ventricular tissue slices were approved by the Institutional Review Board at Northwestern University. Left ventricular slices were generated as previously described (70) using a precision vibrating microtome in an ice-cold slicing solution [140 mM NaCl, 6 mM KCl, 1 mM MgCl₂, 1.8 mM CaCl₂, 10 mM glucose, 10 mM Hepes, and 10 mM 2,3-

butanedionemonoxime (pH 7.4) at 4°C]. The experimental setup is shown in fig. S16. Slices were then allowed to recover at room temperature in a recovery solution [140 mM NaCl, 4.5 mM KCl, 1 mM MgCl₂, 1.8 mM CaCl₂, 10 mM glucose, and 10 mM Hepes (pH 7.4) at room temperature] for at least 20 min before transferring to a bath at 37°C and superfused with a modified Tyrode's solution [128.2 mM NaCl, 20 mM NaHCO₃, 1.19 mM NaH₂PO₄, 4.7 mM KCl, 1.05 mM MgCl₂, 1.3 mM CaCl₂, 11.1 mM glucose, and 10 to 15 mM blebbistatin (pH 7.4) at 37°C]. After a 20-min equilibration period, slices were stained with RH237 for voltage optical mapping. The MEA was positioned on the slice in the field of view of the camera. Slices were paced using a Pt bipolar electrode placed adjacent to the device at 1.5× amplitude of the threshold of stimulation. Optical traces were analyzed using a custom MATLAB software, Rhythm 3.0.

In vivo electrical mapping

Sprague-Dawley rats were anesthetized by 1 to 3% isoflurane inhalation until there was no response to a toe pinch. The rat was intubated and placed on pressure control ventilation in the right lateral decubitus position. Animal ventilation was provided by the VentElite small animal ventilator (Harvard Apparatus, Holliston, MA). ECG leads were connected for cardiac monitoring (lead II configuration). The left lateral chest was shaved and palpated to identify the intercostal space where the point of maximum impulse could best be palpated. Scissors were used to make an incision through the skin and dissect the chest wall muscles to expose the thoracic cavity with care taken not to injure the lung. A rib spreader was used to open the intercostal space. A cotton swab was used to gently retract the lung to expose the heart. Another cotton swab was used to gently remove the pericardium. AV block was induced as previously reported (71). Briefly, animals received (intraperitoneally) caffeine (120 mg/kg; Millipore Sigma, catalog number C0750) and dobutamine (60 mg/kg; Cayman, catalog number 15582) sequentially. Fast pacing (cycle length, 100 ms) was applied to the left ventricle for about 15 min after drug treatment until an AV block was induced. The Mo nanogrid MEA was laid over the heart, covering the front-lateral side of the left ventricle. The MEA was connected to a data acquisition system (PowerLab 16/35, ADInstruments Inc.) with a sampling frequency of 20 kHz. For cardiac pacing purposes, customized Pt bipolar electrodes or the MEA were used to pace the heart from the left ventricle at rates higher than the intrinsic sinus rhythm of the heart. Electrical stimulation amplitude (i.e., pacing voltage) was set at 2× the pacing threshold. Rats were euthanized after experiments. Cervical dislocation and heart extraction were performed after confirmation of no response to a toe pinch.

Supplementary Materials

This PDF file includes:

Figs. S1 to S16 Tables S1 and S2 Legends for movies S1 to S3

Other Supplementary Material for this manuscript includes the following:
Movies S1 to S3

REFERENCES AND NOTES

- S. S. Virani, A. Alonso, E. J. Benjamin, M. S. Bittencourt, C. W. Callaway, A. P. Carson, A. M. Chamberlain, A. R. Chang, S. Cheng, F. N. Delling, L. Djousse, M. S. V. Elkind, J. F. Ferguson, M. Fornage, S. S. Khan, B. M. Kissela, K. L. Knutson, T. W. Kwan, D. T. Lackland, T. T. Lewis, J. H. Lichtman, C. T. Longenecker, M. S. Loop, P. L. Lutsey, S. S. Martin, K. Matsushita, A. E. Moran, M. E. Mussolino, A. M. Perak, W. D. Rosamond, G. A. Roth, U. K. A. Sampson, G. M. Satou, E. B. Schroeder, S. H. Shah, C. M. Shay, N. L. Spartano, A. Stokes, D. L. Tirschwell, L. B. VanWagner, C. W. Tsao, Heart disease and stroke statistics— 2020 update: A report from the American Heart Association. *Circulation* 141, e139–e596 (2020).
- C. D. Fryar, T. C. Chen, X. Li, Prevalence of uncontrolled risk factors for cardiovascular disease: United States, 1999-2010. NCHS Data Brief, 1–8 (2012).
- R. G. Trohman, M. H. Kim, S. L. Pinski, Cardiac pacing: The state of the art. Lancet 364, 1701–1719 (2004).
- M. E. Spira, A. Hai, Multi-electrode array technologies for neuroscience and cardiology. Nat. Nanotechnol. 8, 83–94 (2013).
- J. S. Choi, H. J. Lee, S. Rajaraman, D.-H. Kim, Recent advances in three-dimensional microelectrode array technologies for in vitro and in vivo cardiac and neuronal interfaces. *Biosens. Bioelectron.* 171, 112687 (2021).
- S. A. George, I. R. Efimov, Optocardiography: A review of its past, present, and future. Curr. Opin. Biomed. Eng. 9, 74–80 (2019).
- D. Kuzum, H. Takano, E. Shim, J. C. Reed, H. Juul, A. G. Richardson, J. de Vries, H. Bink, M. A. Dichter, T. H. Lucas, D. A. Coulter, E. Cubukcu, B. Litt, Transparent and flexible low noise graphene electrodes for simultaneous electrophysiology and neuroimaging. *Nat. Commun.* 5, 5259 (2014).
- D.-W. Park, A. A. Schendel, S. Mikael, S. K. Brodnick, T. J. Richner, J. P. Ness, M. R. Hayat, F. Atry, S. T. Frye, R. Pashaie, S. Thongpang, Z. Ma, J. C. Williams, Graphene-based carbonlayered electrode array technology for neural imaging and optogenetic applications. *Nat. Commun.* 5, 5258 (2014).
- J. Zhang, X. Liu, W. Xu, W. Luo, M. Li, F. Chu, L. Xu, A. Cao, J. Guan, S. Tang, X. Duan, Stretchable transparent electrode arrays for simultaneous electrical and optical interrogation of neural circuits in vivo. *Nano Lett.* 18, 2903–2911 (2018).
- Y. U. Cho, J. Y. Lee, U.-J. Jeong, S. H. Park, S. L. Lim, K. Y. Kim, J. W. Jang, J. H. Park, H. W. Kim, H. Shin, H. Jeon, Y. M. Jung, I.-J. Cho, K. J. Yu, Ultra-low cost, facile fabrication of transparent neural electrode array for electrocorticography with photoelectric artifact-free optogenetics. *Adv. Funct. Mater.* 32, 2105568 (2022).
- Y. Qiang, P. Artoni, K. J. Seo, S. Culaclii, V. Hogan, X. Zhao, Y. Zhong, X. Han, P.-M. Wang, Y.-K. Lo, Y. Li, H. A. Patel, Y. Huang, A. Sambangi, J. S. V. Chu, W. Liu, M. Fagiolini, H. Fang, Transparent arrays of bilayer-nanomesh microelectrodes for simultaneous electrophysiology and two-photon imaging in the brain. Sci. Adv. 4, eaat0626 (2018).
- S. N. Obaid, R. T. Yin, J. Tian, Z. Chen, S. W. Chen, K. B. Lee, N. Boyajian, A. N. Miniovich, I. R. Efimov, L. Lu, Multifunctional flexible biointerfaces for simultaneous colocalized optophysiology and electrophysiology. *Adv. Funct. Mater.* 30, 1910027 (2020).
- L. Lu, Recent progress on transparent microelectrode-based soft bioelectronic devices for neuroscience and cardiac research. ACS Appl. Bio Mater. 6, 1701–1719 (2023).
- T.-K. Nguyen, S. Yadav, T.-A. Truong, M. Han, M. Barton, M. Leitch, P. Guzman, T. Dinh, A. Ashok, H. Vu, V. Dau, D. Haasmann, L. Chen, Y. Park, T. N. Do, Y. Yamauchi, J. A. Rogers, N.-T. Nguyen, H.-P. Phan, Integrated, transparent silicon carbide electronics and sensors for radio frequency biomedical therapy. ACS Nano 16, 10890–10903 (2022).
- A. L. Waldo, J. L. Wells, T. B. Cooper, W. A. H. MacLean, Temporary cardiac pacing: Applications and techniques in the treatment of cardiac arrhythmias. *Prog. Cardiovasc. Dis.* 23, 451–474 (1981).
- H. S. Kazaure, S. A. Roman, R. A. Rosenthal, J. A. Sosa, Cardiac arrest among surgical patients: An analysis of incidence, patient characteristics, and outcomes in ACS-NSQIP. *JAMA Surg.* 148, 14–21 (2013).
- R. G. Hauser, W. T. Katsiyiannis, C. C. Gornick, A. K. Almquist, L. M. Kallinen, Deaths and cardiovascular injuries due to device-assisted implantable cardioverter–defibrillator and pacemaker lead extraction. *Europace* 12, 395–401 (2010).
- S.-K. Kang, J. Koo, Y. K. Lee, J. A. Rogers, Advanced materials and devices for bioresorbable electronics. Acc. Chem. Res. 51, 988–998 (2018).
- H. Ryu, M.-H. Seo, J. A. Rogers, Bioresorbable metals for biomedical applications: From mechanical components to electronic devices. Adv. Healthc. Mater. 10, 2002236 (2021).
- Y. S. Choi, H. Jeong, R. T. Yin, R. Avila, A. Pfenniger, J. Yoo, J. Y. Lee, A. Tzavelis, Y. J. Lee,
 W. Chen, H. S. Knight, S. Kim, H.-Y. Ahn, G. Wickerson, A. Vázquez-Guardado, E. Higbee-Dempsey, B. A. Russo, M. A. Napolitano, T. J. Holleran, L. A. Razzak, A. N. Miniovich, G. Lee,
 B. Geist, B. Kim, S. Han, J. A. Brennan, K. Aras, S. S. Kwak, J. Kim, E. A. Waters, X. Yang,
 A. Burrell, K. San Chun, C. Liu, C. Wu, A. Y. Rwei, A. N. Spann, A. Banks, D. Johnson,
 Z. J. Zhang, C. R. Haney, S. H. Jin, A. V. Sahakian, Y. Huang, G. D. Trachiotis, B. P. Knight,

- R. K. Arora, I. R. Efimov, J. A. Rogers, A transient, closed-loop network of wireless, body-integrated devices for autonomous electrotherapy. *Science* **376**, 1006–1012 (2022).
- Y. S. Choi, R. T. Yin, A. Pfenniger, J. Koo, R. Avila, K. Benjamin Lee, S. W. Chen, G. Lee, G. Li, Y. Qiao, A. Murillo-Berlioz, A. Kiss, S. Han, S. M. Lee, C. Li, Z. Xie, Y.-Y. Chen, A. Burrell, B. Geist, H. Jeong, J. Kim, H.-J. Yoon, A. Banks, S.-K. Kang, Z. J. Zhang, C. R. Haney, A. V. Sahakian, D. Johnson, T. Efimova, Y. Huang, G. D. Trachiotis, B. P. Knight, R. K. Arora, I. R. Efimov, J. A. Rogers, Fully implantable and bioresorbable cardiac pacemakers without leads or batteries. Nat. Biotechnol. 39, 1228–1238 (2021).
- G. Lee, E. Ray, H.-J. Yoon, S. Genovese, Y. S. Choi, M.-K. Lee, S. Şahin, Y. Yan, H.-Y. Ahn, A. J. Bandodkar, J. Kim, M. Park, H. Ryu, S. S. Kwak, Y. H. Jung, A. Odabas, U. Khandpur, W. Z. Ray, M. R. MacEwan, J. A. Rogers, A bioresorbable peripheral nerve stimulator for electronic pain block. *Sci. Adv.* 8, eabp9169 (2022).
- K. J. Yu, D. Kuzum, S.-W. Hwang, B. H. Kim, H. Juul, N. H. Kim, S. M. Won, K. Chiang, M. Trumpis, A. G. Richardson, H. Cheng, H. Fang, M. Thompson, H. Bink, D. Talos, K. J. Seo, H. N. Lee, S.-K. Kang, J.-H. Kim, J. Y. Lee, Y. Huang, F. E. Jensen, M. A. Dichter, T. H. Lucas, J. Viventi, B. Litt, J. A. Rogers, Bioresorbable silicon electronics for transient spatiotemporal mapping of electrical activity from the cerebral cortex. *Nat. Mater.* 15, 782–791 (2016).
- H. Zhao, Z. Xue, X. Wu, Z. Wei, Q. Guo, M. Xu, C. Qu, C. You, Y. Mei, M. Zhang, Z. Di, Q. Guo, Biodegradable germanium electronics for integrated biosensing of physiological signals. npj Flex Electron. 6, 63 (2022).
- J. W. Song, H. Ryu, W. Bai, Z. Xie, A. Vázquez-Guardado, K. Nandoliya, R. Avila, G. Lee, Z. Song, J. Kim, M.-K. Lee, Y. Liu, M. Kim, H. Wang, Y. Wu, H.-J. Yoon, S. S. Kwak, J. Shin, K. Kwon, W. Lu, X. Chen, Y. Huang, G. A. Ameer, J. A. Rogers, Bioresorbable, wireless, and battery-free system for electrotherapy and impedance sensing at wound sites. *Nat. Commun.* 9, eade4687 (2023).
- R. Li, H. Qi, Y. Ma, Y. Deng, S. Liu, Y. Jie, J. Jing, J. He, X. Zhang, L. Wheatley, C. Huang, X. Sheng, M. Zhang, L. Yin, A flexible and physically transient electrochemical sensor for real-time wireless nitric oxide monitoring. *Nat. Commun.* 11, 3207 (2020).
- S. N. Obaid, Z. Chen, M. Madrid, Z. Lin, J. Tian, C. Humphreys, J. Adams, N. Daza, J. Balansag, I. R. Efimov, L. Lu, Flexible electro-optical arrays for simultaneous multi-site colocalized spatiotemporal cardiac mapping and modulation. *Adv. Opt. Mater.* 10, 2201331 (2022).
- S. N. Obaid, N. Quirion, J. D. Torres Balansag, N. Daza, X. Shi, Z. Chen, L. Lu, Design and fabrication of a flexible opto-electric biointerface for multimodal optical fluorescence and electrical recording. ACS Appl. Electron. Mater. 5, 1688–1696 (2023).
- E. Entcheva, M. W. Kay, Cardiac optogenetics: A decade of enlightenment. *Nat. Rev. Cardiol.* 18, 349–367 (2021).
- A. Prominski, J. Shi, P. Li, J. Yue, Y. Lin, J. Park, B. Tian, M. Y. Rotenberg, Porosity-based heterojunctions enable leadless optoelectronic modulation of tissues. *Nat. Mater.* 21, 647–655 (2022).
- Z. Lin, D. Kireev, N. Liu, S. Gupta, J. LaPiano, S. N. Obaid, Z. Chen, D. Akinwande, I. R. Efimov, Graphene biointerface for cardiac arrhythmia diagnosis and treatment. *Adv. Mater.* 35, e2212190 (2023).
- R. Parameswaran, K. Koehler, M. Y. Rotenberg, M. J. Burke, J. Kim, K.-Y. Jeong, B. Hissa, M. D. Paul, K. Moreno, N. Sarma, T. Hayes, E. Sudzilovsky, H.-G. Park, B. Tian, Optical stimulation of cardiac cells with a polymer-supported silicon nanowire matrix. *Proc. Natl. Acad. Sci. U.S.A.* 116, 413–421 (2019).
- A. Alex, A. Li, R. E. Tanzi, C. Zhou, Optogenetic pacing in *Drosophila melanogaster. Sci. Adv.* e1500639 (2015).
- A. Savchenko, V. Cherkas, C. Liu, G. B. Braun, A. Kleschevnikov, Y. I. Miller, E. Molokanova, Graphene biointerfaces for optical stimulation of cells. Sci. Adv. 4, eaat0351 (2018).
- U. Nussinovitch, L. Gepstein, Optogenetics for in vivo cardiac pacing and resynchronization therapies. Nat. Biotechnol. 33, 750–754 (2015).
- H. Ouyang, Z. Li, M. Gu, Y. Hu, L. Xu, D. Jiang, S. Cheng, Y. Zou, Y. Deng, B. Shi, W. Hua, Y. Fan, Z. Li, Z. Wang, A bioresorbable dynamic pressure sensor for cardiovascular postoperative care. Adv. Mater. 33, 2102302 (2021).
- R. Li, L. Wang, D. Kong, L. Yin, Recent progress on biodegradable materials and transient electronics. *Bioact. Mater.* 3, 322–333 (2018).
- C. Cabo, R. C. Barr, Unidirectional block in a computer model of partially coupled segments of cardiac Purkinje tissue. Annu. Rev. Biomed. Eng. 21, 633–644 (1993).
- K. A. Collins, C. E. Korcarz, S. G. Shroff, J. E. Bednarz, R. C. Fentzke, H. Lin, J. M. Leiden, R. M. Lang, Accuracy of echocardiographic estimates of left ventricular mass in mice. Am. J. Physiol. Heart Circ. Physiol. 280, H1954–H1962 (2001).
- W. Liu, M. W. Ashford, J. Chen, M. P. Watkins, T. A. Williams, S. A. Wickline, X. Yu, MR tagging demonstrates quantitative differences in regional ventricular wall motion in mice, rats, and men. Am. J. Physiol. Heart Circ. Physiol. 291, H2515–H2521 (2006).
- S.-K. Kang, S.-W. Hwang, S. Yu, J.-H. Seo, E. A. Corbin, J. Shin, D. S. Wie, R. Bashir, Z. Ma, J. A. Rogers, Biodegradable thin metal foils and spin-on glass materials for transient electronics. Adv. Funct. Mater. 25. 1789–1797 (2015).

SCIENCE ADVANCES | RESEARCH ARTICLE

- C. Li, C. Guo, V. Fitzpatrick, A. Ibrahim, M. J. Zwierstra, P. Hanna, A. Lechtig, A. Nazarian, S. J. Lin, D. L. Kaplan, Design of biodegradable, implantable devices towards clinical translation. *Nat. Rev. Mater.* 5, 61–81 (2020).
- P. Trumbo, A. A. Yates, S. Schlicker, M. Poos, Dietary reference intakes: Vitamin A, vitamin K, arsenic, boron, chromium, copper, iodine, iron, manganese, molybdenum, nickel, silicon, vanadium, and zinc. J. Am. Diet. Assoc. 101, 294

 –301 (2001).
- H. K. Makadia, S. J. Siegel, Poly Lactic-co-Glycolic Acid (PLGA) as biodegradable controlled drug delivery carrier. *Polymers* 3, 1377–1397 (2011).
- N. Kunori, I. Takashima, A transparent epidural electrode array for use in conjunction with optical imaging. J. Neurosci. Methods 251, 130–137 (2015).
- M. Thunemann, Y. Lu, X. Liu, K. Kılıç, M. Desjardins, M. Vandenberghe, S. Sadegh, P. A. Saisan, Q. Cheng, K. L. Weldy, H. Lyu, S. Djurovic, O. A. Andreassen, A. M. Dale, A. Devor, D. Kuzum, Deep 2-photon imaging and artifact-free optogenetics through transparent graphene microelectrode arrays. *Nat. Commun.* 9, 2035 (2018).
- M. Ganji, A. Tanaka, V. Gilja, E. Halgren, S. A. Dayeh, Scaling effects on the electrochemical stimulation performance of Au, Pt, and PEDOT:PSS electrocorticography arrays. Adv. Funct. Mater. 27, 1703019 (2017).
- M. Ganji, A. T. Elthakeb, A. Tanaka, V. Gilja, E. Halgren, S. A. Dayeh, Scaling effects on the electrochemical performance of poly(3,4-ethylenedioxythiophene (PEDOT), Au, and Pt for electrocorticography recording. Adv. Funct. Mater. 27, 1703018 (2017).
- J. D. Weiland, D. J. Anderson, M. S. Humayun, In vitro electrical properties for iridium oxide versus titanium nitride stimulating electrodes. *IEEE. Trans. Biomed. Eng.* 49, 1574–1579 (2002)
- W. Yang, A. Broski, J. Wu, Q. H. Fan, W. Li, Characteristics of transparent, PEDOT:PSS-coated indium-tin-oxide (ITO) microelectrodes. *IEEE Trans. Nanotechnol.* 17, 701–704 (2018).
- W. Sugimoto, K. Aoyama, T. Kawaguchi, Y. Murakami, Y. Takasu, Kinetics of CH₃OH oxidation on PtRu/C studied by impedance and CO stripping voltammetry. J. Electroanal. Chem. 576, 215–221 (2005).
- J.-M. Hu, J.-T. Zhang, J.-Q. Zhang, C.-N. Cao, Corrosion electrochemical characteristics of red iron oxide pigmented epoxy coatings on aluminum alloys. *Corros. Sci.* 47, 2607–2618 (2005).
- Z. Chen, N. Boyajian, Z. Lin, R. T. Yin, S. N. Obaid, J. Tian, J. A. Brennan, S. W. Chen, A. N. Miniovich, L. Lin, Y. Qi, X. Liu, I. R. Efimov, L. Lu, Flexible and transparent metal nanowire microelectrode arrays and interconnects for electrophysiology, optogenetics, and optical mapping. *Adv. Mater. Technol.* 6, 2100225 (2021).
- W. F. DeForge, Cardiac pacemakers: A basic review of the history and current technology.
 J. Vet. Cardiol. 22, 40–50 (2019).
- H. Beck, W. E. Boden, S. Patibandla, D. Kireyev, V. Gupta, F. Campagna, M. E. Cain, J. E. Marine, 50th anniversary of the first successful permanent pacemaker implantation in the United States: Historical review and future directions. *Am. J. Cardiol.* 106, 210–219 (2010)
- S. K. Mulpuru, M. Madhavan, C. J. McLeod, Y.-M. Cha, P. A. Friedman, Cardiac pacemakers: Function, troubleshooting, and management: Part 1 of a 2-part series. *J. Am. Coll. Cardiol.* 69, 189–210 (2017).
- 57. J. M. Mangrum, J. P. DiMarco, The evaluation and management of bradycardia. *N. Engl.*
- S. Sidhu, J. E. Marine, Evaluating and managing bradycardia. *Trends Cardiovasc. Med.* 30, 265–272 (2020).
- Q. Yang, T. Wei, R. T. Yin, M. Wu, Y. Xu, J. Koo, Y. S. Choi, Z. Xie, S. W. Chen, I. Kandela, S. Yao, Y. Deng, R. Avila, T.-L. Liu, W. Bai, Y. Yang, M. Han, Q. Zhang, C. R. Haney, K. Benjamin Lee, K. Aras, T. Wang, M.-H. Seo, H. Luan, S. M. Lee, A. Brikha, N. Ghoreishi-Haack, L. Tran, I. Stepien, F. Aird, E. A. Waters, X. Yu, A. Banks, G. D. Trachiotis, J. M. Torkelson, Y. Huang,

- Y. Kozorovitskiy, I. R. Efimov, J. A. Rogers, Photocurable bioresorbable adhesives as functional interfaces between flexible bioelectronic devices and soft biological tissues. *Nat. Mater.* **20**, 1559–1570 (2021).
- J. Liu, X. Zhang, Y. Liu, M. Rodrigo, P. D. Loftus, J. Aparicio-Valenzuela, J. Zheng, T. Pong, K. J. Cyr, M. Babakhanian, J. Hasi, J. Li, Y. Jiang, C. J. Kenney, P. J. Wang, A. M. Lee, Z. Bao, Intrinsically stretchable electrode array enabled in vivo electrophysiological mapping of atrial fibrillation at cellular resolution. *Proc. Natl. Acad. Sci. U.S.A.* 117, 14769–14778 (2020).
- Z. Xiang, H. Wang, J. Wan, L. Miao, C. Xu, P. Zhao, H. Guo, H. Zhang, M. Han, High-density stretchable microelectrode array based on multilayer serpentine interconnections. J. Micromech. Microeng. 32, 084002 (2022).
- R. T. Yin, S. W. Chen, K. Benjamin Lee, Y. S. Choi, J. Koo, Q. Yang, M. A. Napolitano, J. Ausra, T. J. Holleran, J. B. Lapiano, E. Alex Waters, A. Brikha, G. Kowalik, A. N. Miniovich, H. S. Knight, B. A. Russo, A. Kiss, A. Murillo-Berlioz, T. Efimova, C. R. Haney, P. Gutruf, J. A. Rogers, G. D. Trachiotis, I. R. Efimov, Open thoracic surgical implantation of cardiac pacemakers in rats. *Nat. Protoc.* 18, 374–395 (2023).
- M. Rienks, A.-P. Papageorgiou, N. G. Frangogiannis, S. Heymans, Myocardial extracellular matrix. Circ. Res. 114, 872–888 (2014).
- R. J. Perea, J. T. Ortiz-Perez, M. Sole, M. T. Cibeira, T. M. de Caralt, S. Prat-Gonzalez, X. Bosch, A. Berruezo, M. Sanchez, J. Blade, T1 mapping: Characterisation of myocardial interstitial space. *Insights Imaging* 6, 189–202 (2015).
- S. P. Murphy, N. E. Ibrahim, J. L. Januzzi Jr., Heart failure with reduced ejection fraction: A review. JAMA 324, 488–504 (2020).
- U. Laufs, K. G. Parhofer, H. N. Ginsberg, R. A. Hegele, Clinical review on triglycerides. Eur. Heart J. 41, 99–109c (2020).
- J. K. Limdi, G. M. Hyde, Evaluation of abnormal liver function tests. *Postgrad. Med. J.* 79, 307–312 (2003).
- A. S. Levey, R. D. Perrone, N. E. Madias, Serum creatinine and renal function. *Annu. Rev. Med.* 39, 465–490 (1988).
- S. A. George, Z. Lin, I. R. Efimov, Simultaneous triple-parametric optical mapping of transmembrane potential, intracellular calcium and NADH for cardiac physiology assessment. Commun. Biol. 5, 319 (2022).
- S. A. George, J. A. Brennan, I. R. Efimov, Preclinical cardiac electrophysiology assessment by dual voltage and calcium optical mapping of human organotypic cardiac slices. *J. Vis. Exp.* 160, e60781 (2020).
- C. Zhang, Y. Zhang, Caffeine and dobutamine challenge induces bidirectional ventricular tachycardia in normal rats. *Heart Rhythm* 1, 359–367 (2020).

Acknowledgments

Funding: This project was supported by the NSF (2011093 and 2131682 to L.L. and I.R.E.) and the NIH (R01 HL141470 to I.R.E.). **Author contributions:** Conceptualization: Z.C., Z.L., I.R.E., and L.L. Methodology: Z.C., Z.L., and J.L. Investigation: Z.C., Z.L., S.N.O., E.R., S.A.G., C.B., M.M., B.R., and H.K. Fabrication: Z.C., C.B., M.L., A.F., X.S., N.Q., and A.A. Visualization: Z.C., Z.L., and S.A.G. Supervision: I.R.E. and L.L. Writing: Z.C., Z.L., I.R.E., and L.L. **Competing interests:** The authors declare that they have no competing interests. **Data and materials availability:** All data needed to evaluate the conclusions in the paper are present in the paper and/or the Supplementary Materials.

Submitted 1 April 2023 Accepted 1 June 2023 Published 5 July 2023 10.1126/sciady.adi0757

Downloaded from https://www.science.org on January 17, 2024

Science Advances

Soft, bioresorbable, transparent microelectrode arrays for multimodal spatiotemporal mapping and modulation of cardiac physiology

Zhiyuan Chen, Zexu Lin, Sofian N. Obaid, Eric Rytkin, Sharon A. George, Christopher Bach, Micah Madrid, Miya Liu, Jessica LaPiano, Amy Fehr, Xinyu Shi, Nathaniel Quirion, Benjamin Russo, Helen Knight, Anthony Aduwari, Igor R. Efimov, and Luyao Lu

Sci. Adv. 9 (27), eadi0757. DOI: 10.1126/sciadv.adi0757

View the article online

https://www.science.org/doi/10.1126/sciadv.adi0757 **Permissions**

https://www.science.org/help/reprints-and-permissions

Use of this article is subject to the Terms of service